

Experimental Study and Analysis of Light Scattering Patterns of Bragg Fibers Fabricated in PECVD

Zeba Naqvi (✉ naqvi.zeba@gmail.com)

Ansys Inc <https://orcid.org/0000-0003-3518-5159>

Tsing-Hua Her

University of North Carolina at Charlotte

Research Article

Keywords: Analysis, Mie Scattering, Bragg Fibers

Posted Date: September 23rd, 2021

DOI: <https://doi.org/10.21203/rs.3.rs-879365/v1>

License:   This work is licensed under a Creative Commons Attribution 4.0 International License.

[Read Full License](#)

Experimental Study and Analysis of Mie Scattering of Bragg Fibers

ZEBNA NAQVI^{1,2,*} AND TSING-HUA HER¹

¹Department of Physics and Optical Science, University of North Carolina at Charlotte, 9203 University City Blvd, Charlotte, NC 28223, USA

²Ansys Canada Ltd., 283 Northfield Dr E 21, Waterloo, ON N2J 4G8, Canada

*Corresponding author: zeba.naqvi@ansys.com

Compiled September 4, 2021

Light scattering patterns are commonly used in industry to assess fiber quality. In this work, scattering patterns of Bragg fibers are studied. Optical fibers are coated with alternating layers of Silicon Nitride and Silica using Plasma Enhanced Chemical Vapor Deposition. A laser beam incident perpendicular to the fiber axis scatters off creating patterns distinct from that of uncoated fibers which exhibit continuous front lobe. Effect of variation in layer properties, polarization, wavelength and fiber symmetry is observed in the patterns. Anomalous suppression and enhancement in angular scattering pattern is explained through a scattering angle diagram. Features in the pattern are mapped to reflectance of the Bragg stack and it is found that a stop-band creates the anomalous features in the scattering.

© 2021 Optical Society of America

<http://dx.doi.org/10.1364/ao.XX.XXXXXX>

1. INTRODUCTION

Information contained in the scattering pattern of particles makes its analysis of great interest for both military and civil applications. Modifications such as adding multiple layers to the scatterers adds further richness to their interaction with light. A good understanding of scattering from such particles is essential to tap into their potential for opening new applications. Scattering manipulation by such designer particles for invisibility through scattering suppression [1][2][3][4][5] and mimicking that of another scatterer, is being studied extensively, including efforts to include multi-material fabrication [6]. Though scattering from simple configurations such as single [7][8][9] or bi-layered [10][11] structures have been studied extensively, little work exists on multilayered structures especially using all-dielectric materials. Some theoretical efforts to improve our understanding of scattering from multilayered spheres include work of Liang et al. [12][13], in which Mie scattering of Bragg onion resonators was investigated and Whispering Gallery Modes of the resonator were mapped to a peculiar scattering behavior. In another theoretical work on scattering of Bragg spheres [14], enhancement in backward to forward scattering ratio for large core spheres was reported. In this paper,

its cylindrical counterpart - a Bragg fiber, traditionally used for transmission, is studied as a scatterer, experimentally, alleviating the current lack of experimental work in the area of scattering from multilayered cylinders. The Bragg fibers were fabricated using Plasma Enhanced Chemical Vapor Deposition (PECVD) [15] as described in section 2. Section 3 reports the experimental scattering data and their sensitivity to variation in layer thicknesses. Peculiar suppression and enhancement in the angular scattering pattern was observed for a fiber with particular thickness of Silicon Nitride and Silica layers. A model based on ray tracing is developed in section 4 to explain these features.

2. FABRICATION

A commercial RF-PECVD tool, usually used for deposition on flat substrates, was modified to fabricate Bragg fibers by depositing alternating layers of Silica and Silicon Nitride [15]. Figure 1 shows the schematic of the tool. A rotary feedthrough is attached to a view port on the chamber wall to achieve azimuthal uniformity of layers. The rotary shaft holds a fiber chuck which holds one end of the fiber while the other end rests in a groove in a glass holder placed at the opposite end of the base platen. Precursor gases entering the chamber from the top are directed downward through a showerhead. A 10 inch strand of the fiber from Thorlabs (FT200EMT) is used as the substrate for deposition. It is cleaned by sonication, loaded into the chamber and coated with 12 pairs of SiN_x and SiO_2 , terminating in a $1\text{-}\mu$ thick layer of SiO_2 . An SEM image of the layers coated on a Bragg fiber are shown in Figure 2. The substrate fiber is to the left followed by 12 pairs of Silicon Nitride and Silica, terminating in a thick layer of Silica.

3. SCATTERING DATA

To study the scattering pattern of the fibers, a simple scatterometer was setup using HeNe laser as shown in Figure 3 [15]. Scattering is very sensitive to the symmetry of the substrate fiber as shown in Figure 4 (a) and (f). Uncoated fiber from Thorlabs (FT200EMT) shows some asymmetry while that from Corning (SMF28e+) exhibits highly symmetrical scattering. We used the fiber from Thorlabs due to its large core and used 2 different recipes to create two Bragg fibers - BF1 and BF2. Deposition times for SiN_x and SiO_2 for BF1 were 11 mins 2.33 secs and 36.91 secs respectively while for BF2 we used 8 mins 19.74 secs

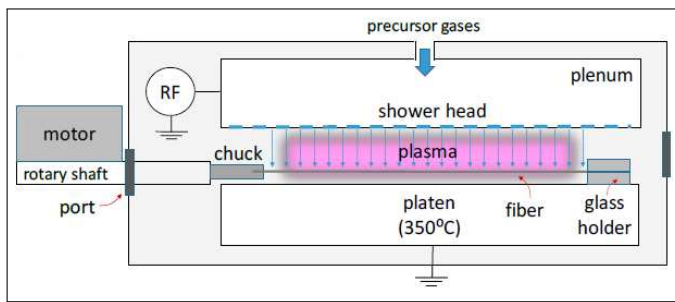


Fig. 1. Schematic of the PECVD chamber with rotary feedthrough attached on the left through a port. The fiber ends are held in a chuck inserted in the rotary shaft and a glass groove.

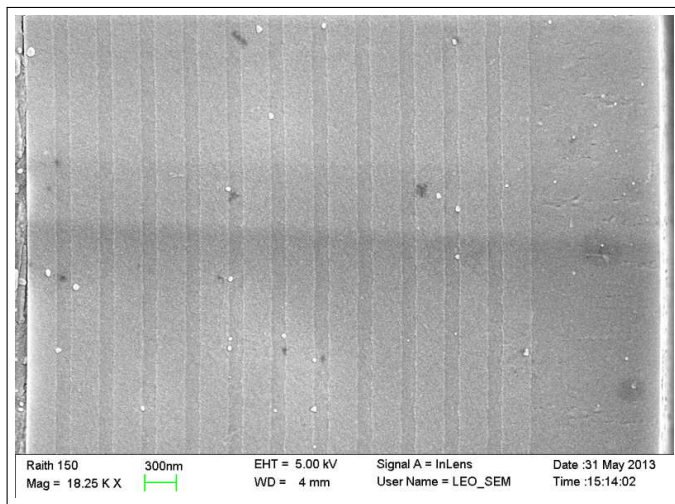


Fig. 2. SEM image of a sample Bragg fiber. Fiber substrate is to the left followed by 12 pairs of SiN_x/SiO_2 coated on the fiber.

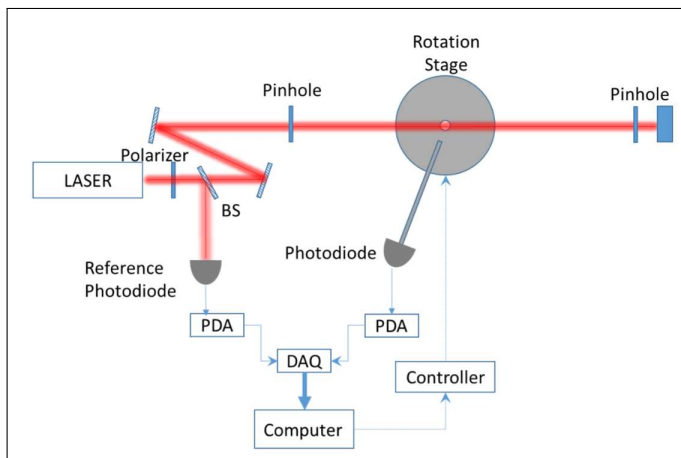


Fig. 3. Schematic of experimental set-up. Fiber is placed at the center of the rotation stage. Computer controls the rotation stage and scattering signal is read through the Data Acquisition Card (DAQ).

and 1 min 49.26 secs respectively. The scattering patterns of the two designs are very different as seen in Figure 4 (b) and (g). For laser polarized perpendicular to fiber axis (TE), the patterns (Figure 4 (c) and (h)) differ only slightly from corresponding patterns using TM polarization. It also depends on the location along the fiber. Pattern in Figure 4 (i) taken from a point that was near the chuck used during deposition to hold the fiber, is very different from that obtained from a point in the middle section which was in the center of the plasma chamber (Figure 4 (d)). The same point probed with 532 nm laser shows a different pattern. See Figure 4 (e) vs (j).

Bragg fiber BF1 behaves much like the bare fiber in that it has a dominant forward scattering lobe and a tail like back scattering, except for periodic modulation in intensity. In contrast to these, BF2 has a peculiar pattern bearing hardly any resemblance to the scattering from bare fiber and BF1. To take a deeper look at the strange behavior of BF2, its scattering data spread out in an XY graph as shown in Figure 5 along with a bare fiber pattern for comparison. The left and right columns correspond to TM ($E \parallel$ to fiber axis) and TE ($E \perp$ to fiber axis) polarizations respectively. The intensity on Y axis has been truncated to make the intricate pattern visible. Bare fiber patterns (Figure 5 (a) and (b)) exhibit pattern decreasing monotonically and approaches zero and remains so until a sharp spike appears. Patterns for the two polarizations differ in the sharpness of transition from dark zone to backscattering, TM being sharper than TE. In contrast, data of the Bragg fiber BF2 (Figure 5 (c) and (d)) is apparently chaotic with no distinct forward and backscattering regions. The main distinctive features in these patterns are: 1) notches followed by drastic suppression in forward scattering in the band of 0° – 40° , 2) enhanced scattering in the otherwise dark zone of bare fiber, 3) a bump between 130° – 150° 4) modified backscattering and 5) narrow dip in scattering around 130° . To explain the origin of these features, a model is developed in the next section.

4. RESULTS AND ANALYSIS

We apply the theory of plane wave scattering from concentric infinite cylinders [16][17] to determine theoretical scattering pattern of Bragg fibers which were illuminated by a collimated HeNe beam during experiment. This requires the values of refractive indexes and thicknesses of the layers. In our previous work [15], these were characterized for single layers deposited on fibers using scattering patterns and SEM. Though work exists on calculating scattering coefficients for non-plane waves [18], there was negligible difference between patterns taken with expanded and not expanded beams. Since the pattern is very sensitive to the properties of the layers, we search for the values of thickness and refractive index of the layers that match best with the experimental data in the neighborhood of the values determined in [15]. Due to high number of concentric cylinders, best-fit pattern was found manually by tweaking the values, as the peculiar pattern of Bragg Fiber made the search easier. As the scattering pattern is not very sensitive to variation in core diameter and terminal layer thickness, core diameter was fixed at $200 \mu\text{m}$ and terminal layer thickness to $1 \mu\text{m}$, respectively, to reduce the search parameters.

The best fit patterns obtained by manual search shown in Figure 6 (b) and (d), match reasonably with overall profile of experimental data in Figure 6 (a) and (c). The best-fitted layer thicknesses for SiN_x and SiO_2 are 166 nm and 375 nm, respectively, which are within the error bar of SEM based growth rate

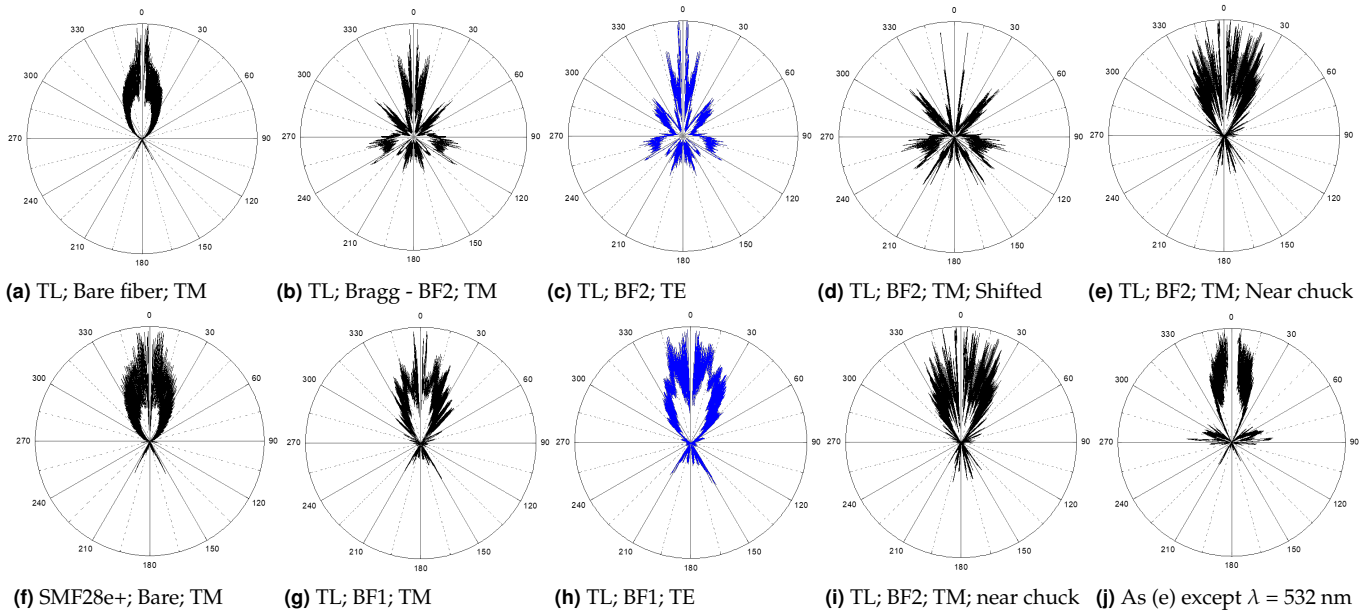


Fig. 4. Sensitivity of scattering pattern of fibers to azimuthal symmetry, recipe, polarization, location on fiber hence thickness, and wavelength - (a) uncoated Thorlabs(TL) FT200EMT (b) Bragg fiber BF2 using TL (f) uncoated Corning SMF28e+ (c) BF2 using TE polarization (d) BF2 but probed in the transition area (e) BF2 probed near end close to chuck (g)BF1 (h) BF1 using TE polarization (i) same as (e) (j) same spot probed as in (e) with green microchip laser (532 nm). All data obtained using TM polarization except (c) and (h), and use HeNe laser except (j).

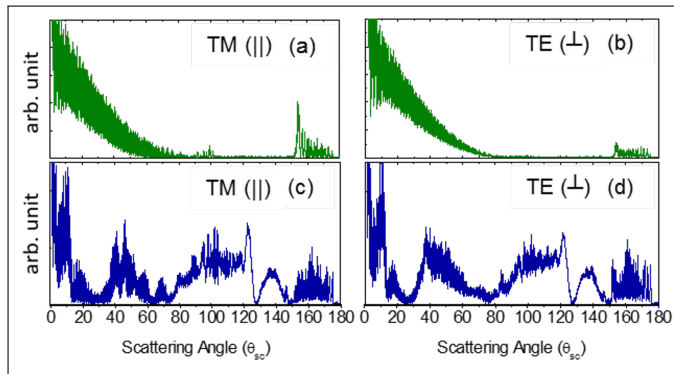


Fig. 5. Modification of scattering pattern due to Bragg layers coated on fiber: (a)-(b) pattern created by bare fiber using TM and TE polarization respectively, (c)-(d) pattern created by Bragg fiber BF2 using TM and TE polarization respectively.

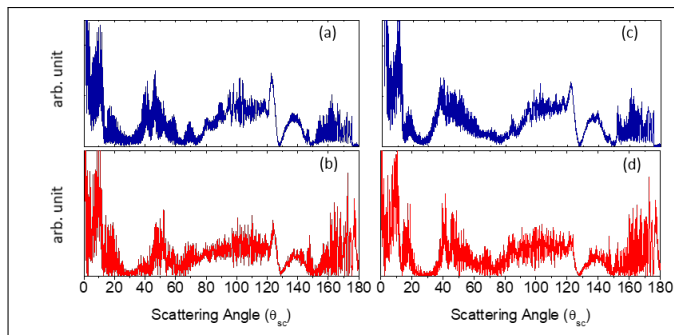


Fig. 6. Experimental scattering data ((a), (c)) vs theoretical fit ((b),(d)) for Bragg fiber 2 using TM (left) and TE (right) polarization.

calibration curve [5]. The best fit refractive index values for SiNx and SiO₂ are 2.495 and 1.608, respectively which are higher than that on flat wafer using same recipe, which is 1.98 for SiN_x and 1.47 for SiO₂. Scattering patterns in Figure 7 (c) and (f) generated numerically using refractive index values corresponding to flat wafers, look nothing like the experimental data (Figure 7 (a) and (d)), further ascertaining the increase in RI due to changed growth kinetics on rotating fiber. Now we use the best fit values of index and thickness to explain the departure of scattering pattern of BF from that of uncoated fiber. Since fiber diameter is much larger than HeNe wavelength, ray tracing approach is used. We develop a scattering angle (θ_{sc}) vs incidence angle (θ_{in}) diagram. In a pencil of rays incident normal to the fiber axis, the angle of incidence varies from 0° to 90° with respect to local normal at the air-fiber interface. One incident ray is shown in Figure 8 as an example. Out of the infinite scattered rays generated by this incident ray, only the first three, marked as Ray1, Ray2, Ray3 at 1st, 2nd and 3rd interface respectively are considered. Scattering angle of Ray_i is measured from the incidence direction and is given by

$$\theta_{sc}^{(1)} = 180 - 2\theta_{in}, \quad (1)$$

$$\theta_{sc}^{(2)} = 2(\theta_{in} - \theta_r), \quad (2)$$

$$\theta_{sc}^{(3)} = 180 + 2\theta_{in} - 4\theta_r, \quad (3)$$

for each ray. Here θ_r is the refraction angle. The scattering angle diagram for the 3 rays as a function of incidence angle is plotted in Figure 8 (b). From this diagram it is easy to read out the rays contributing at a given scattering angle. Region of scattering angle 0°–100° receives rays 1 with between 50°–90° and rays 2 with from 0°–90°, while (100°–150°) receives only rays 1 with roughly between 17°–40°. Backscattering range 150°–180° is formed by superposition of Ray1 and Ray3. Ray3 with at least

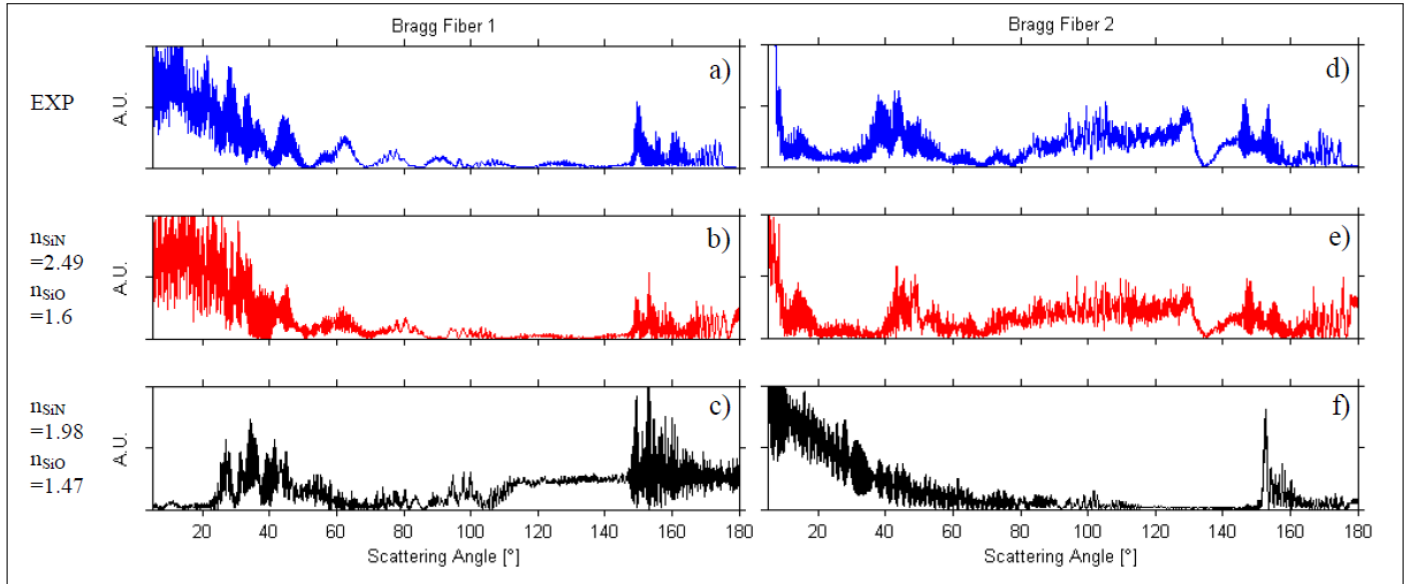


Fig. 7. Scattering of Bare fiber modified by Bragg layers: pattern for (a) bare fiber (TM), (b) bare fiber (TE), Bragg fiber (TM), Bragg fiber (TE).

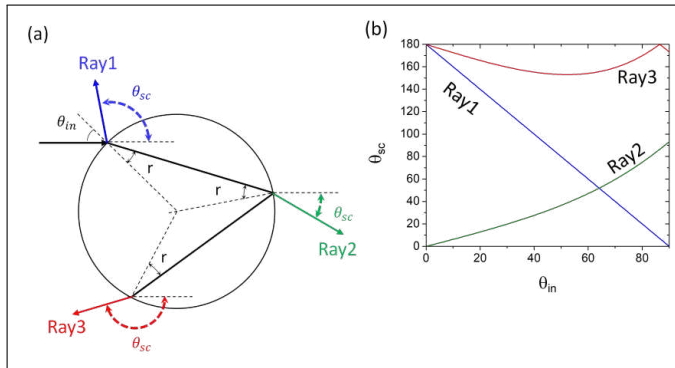


Fig. 8. (a) Rays generated by a given incident ray making θ_{in} at air fiber interface: Ray1 - first reflected ray, Ray2 - ray transmitted, Ray3 - second reflected ray. Scattering angle for each ray is marked as θ_{sc} . (b) Scattering angle vs incidence angle for the three rays.

two incidence angles contribute at a given scattering angle, a point missed by Presby [6] but later corrected by Marcuse [7], elucidating the utility of these plots. Note the wrapping of the curve of Ray3 beyond $\theta_{in} \approx 85^\circ$ where θ_{sc} reaches 180° . This cross-over incidence angle is inversely proportional to RI of fiber.

This diagram is independent of radius of the fiber but depends on the refractive index. The curve of Ray3 as well as Ray2 depends on the index. The minimum for Ray3 also called the cut-off angle, was used to characterize fiber index by Presby [6]. The information about the fiber diameter is contained in interference between these rays. The separation between fringes was used to find the diameter of the fiber in [7]. However here we are concerned with scattering intensity distribution as a function of scattering angle. Neglecting interference, we simply include the information of intensity of each ray. We know from Fresnel reflection coefficients, that intensity I of the rays depends on and the number of interfaces on their trajectory. If R_{af} is the angular reflectance of air-fiber interface, the scattering intensity of the

three types of rays is as follows:

$$I_1 \propto R_{af}(\theta_{in}), \quad (4)$$

$$I_2 \propto (1 - R_{af}(\theta_{in}))(1 - R_{fa}(\theta_r)), \quad (5)$$

$$I_3 \propto (1 - R_{af}(\theta_{in}))R_{fa}(\theta_r)(1 - R_{fa}(\theta_r)), \quad (6)$$

Here the subscripts *af* and *fa* mean air-fiber and fiber-air respectively. Due to reciprocity of the system, $R_{af} = R_{fa} = R$ and equations 4-6 reduce to the following:

$$I_1 \propto R(\theta_{in}), \quad (7)$$

$$I_2 \propto (1 - R(\theta_{in}))^2, \quad (8)$$

$$I_3 \propto R(\theta_{in})(1 - R(\theta_{in}))^2. \quad (9)$$

We will augment the scattering angle diagram in Figure 8 (b) with the intensity information by making line thicknesses of rays 1 – 3 proportional to I_1 , I_2 and I_3 respectively resulting in augmented scattering angle diagrams discussed next for bare and Bragg fibers.

A. Augmented scattering angle diagram for Bare Fiber

Using bare fiber as an example, Figure 9 shows augmented scattering angle diagram for a bare fiber for TM polarization on the left with reflectance plotted below θ_{in} axis and scattering signature of the bare fiber beside the θ_{sc} axis. From the line thicknesses of θ_{sc} vs θ_{in} diagram, the origin of characteristics of forward-scattering, back-scattering and dead-zone become evident. For $\theta_{sc} \in (0,100)$, strongly scattered Ray1 at grazing incidence interfere with strong near-normally incident Ray2 that monotonically decrease in intensity (width of green line i.e. Ray2 is decreasing with incidence angle). This band forms the dominant forward scattering of bare fiber that reduces in intensity with scattering angle. For $\theta_{sc} \in (100, 150)$ – the dead zone, only contribution is from the weakly scattered Ray1. Lastly, $\theta_{sc} \in (150, 180)$ is the well-known backscattering region where only weak Ray1 and Ray3 contribute. Since the Ray3 are weakest due to 3 bounces, the line thickness has been scaled up 4 times

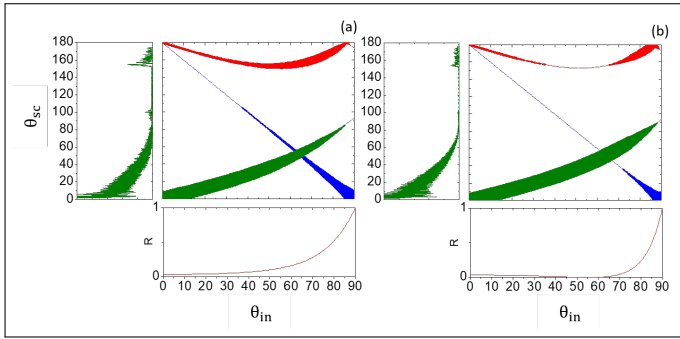


Fig. 9. Scattering angle diagram augmented with intensity information for bare fiber, for electric field parallel (a) and perpendicular (b) to fiber axis.

relative to other 2 curves. Note that the minimum of Ray3 curve at about 150° agrees well with the backscattering cutoff angle of the experimental data along the Y axis. A similar plot for TE polarization shown on the right, visualizes the effect of Brewster's angle clarifying the reason for difference in backscattering cut off.

B. Augmented scattering angle diagram for Bragg Fiber

Now we create augmented scattering angle diagram for Bragg fiber. Two assumptions are made in this analysis for Bragg fiber. Firstly, since the thickness of the Bragg layer is much smaller than the core radius, we neglect its thickness for ray tracing and therefore the skeleton of the diagram remains the same as in Figure 8 and assume that the presence of the Bragg layer modifies only the local reflectance/transmittance at the air-fiber interface. Secondly, since the ratio of fiber diameter and wavelength ($200/0.633$) is very large, the Bragg layers can be assumed to be locally planar. The reflectance from the layers for the two polarizations can be calculated using best fit values obtained resulting in diagrams in Figure 10.

The presence of the wide stopband in reflectance curve, immediately explains the bizarre scattering signature of the Bragg fiber. Stopband blocks corresponding incident rays from entering the fiber stripping a portion of forward scattering. These rays reflected with $R=1$ appear in otherwise dead zone of bare fiber. To facilitate understanding, dashed lines are drawn on the figure as eye-guides while shaded bands have been drawn on the axes to trace the effect of stopband (hatched) and first reflectance peak (gray). Note the suppression of green (Ray2) leads to suppressed forward scattering while enhancement of blue (Ray1) curve leads to complementary enhancement of scattering, both marked with hatched shading and are due to complete stopband. Similar pair of suppression and enhancement can be observed arising from first reflectance peak highlighted traced by gray shading which is narrower and has $R<1$. Being narrower, it suppresses/enhances only narrow portions of scattering as depicted by gray shaded area on the Y axis. The dip in reflectance curve lying between $20 - 30$ degrees traces to spike around $= 19^\circ$ and dip at 130° . Note that even though red curve (Ray3) is suppressed due to stopband, there is no significant effect of this on scattering intensity because it is not a monotonic curve. Therefore scattering arising from rays with incidence angles outside stopband, make up for the suppression.

No stopband in the reflectance curve leads to pattern similar to bare fiber. Such is the case with BF1 (Figure 11) for which the reflectance curve is similar qualitatively to that of air-glass

interface, however with some ripples due to interference in the Bragg layer in passband. More accurate analysis can be done by including the phase of the rays in the model. Shift in the ray trajectories due to thickness of the coated Bragg layers, neglected in this study can further improve the accuracy.

5. CONCLUSION

Theory of plane wave scattering from infinitely long concentric cylinders is used to determine Bragg layers' thicknesses and refractive indexes from experimental scattering data. Despite the departure from ideal case due to surface roughness, possible gaps in the layers, and nonideality of the light source such as impurity of polarization and non-planarity of incident wave, the theory and experiment match reasonably well. The values for the layer thickness and refractive index that produce theoretical patterns closely matching the experimental data, generate angular reflectance curve that maps very well with the features in the scattering pattern. These best-fit values of refractive index for SiN_x and SiO_2 are greater than those of SiN_x/SiO_2 deposited using the same recipe, on flat wafers which the PECVD is originally designed for. Further, we see that the pattern taken from a spot on the fiber that was near the fiber chuck used during deposition, is dramatically different from the pattern obtained from spots that were in the center of the plasma chamber. This is possibly due to the variation in the plasma density in the chamber due to the presence of metallic chuck that holds the fiber, which leads to a gradient in thickness along the fiber axis. Further, the pattern of uncoated Thorlabs fibers is found to be asymmetric unlike highly symmetric pattern of the fibers from Corning. This asymmetry reflects in the pattern of coated fibers as well. Overall, the patterns are sensitive indicators of any variation in layer properties.

Furthermore, the scattering angle diagrams presented in this work, enable understanding the origin of features in the scattering patterns. The diagrams visualize the origin of back scattering cut off and which rays contribute to it, not easy on the first glance and missed in the pioneering work on scattering from optical fibers. Most importantly the diagram immediately reveals that the anomalous pattern of Bragg fiber BF2 is due to the stop band in the reflectance curve of the Bragg stack. No stopband in the reflectance leads to pattern similar to bare fiber with a forward and backscattering region separated by a dark zone as in the case for BF1. The notches where reflectance goes to zero, appear as notches in the scattering pattern.

The sensitivity of the scattering patterns could be utilized further. For example, molecules in contact with the Bragg layers may act as a defect layer possibly modifying the scattering signature and may be explored in the field of sensing.

Declarations

Funding: No funding was received for this work. Conflicts of Interest: Authors declare no conflict of interest. Availability of Data and Material: Available upon request. Code Availability: Not Applicable.

REFERENCES

1. A. Mirzaei, A. E. Miroshnichenko, I. V. Shadrivov, and Y. S. Kivshar, "All-Dielectric Multilayer Cylindrical Structures for Invisibility Cloaking," *Scientific Reports*, vol. 5, p. 9574, 04/10
2. Rybin MV, Filonov DS, Belov PA, Kivshar YS, Limonov MF. Switching from visibility to invisibility via Fano resonances: theory and experiment. *Sci Rep*. 2015.

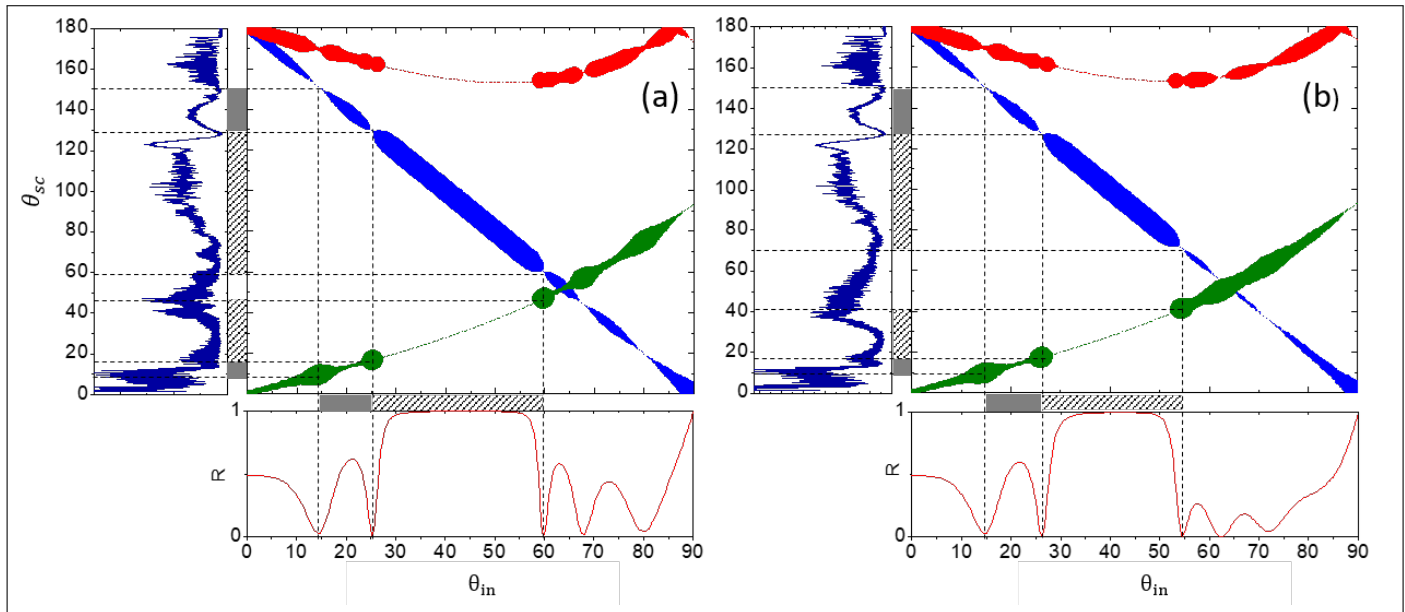


Fig. 10. Augmented scattering angle diagram for Bragg fiber 2 for TM (a) and TE (b) polarizations. Features in the angular reflectance curve of the Bragg layers is mapped onto the resultant features in the scattering pattern.

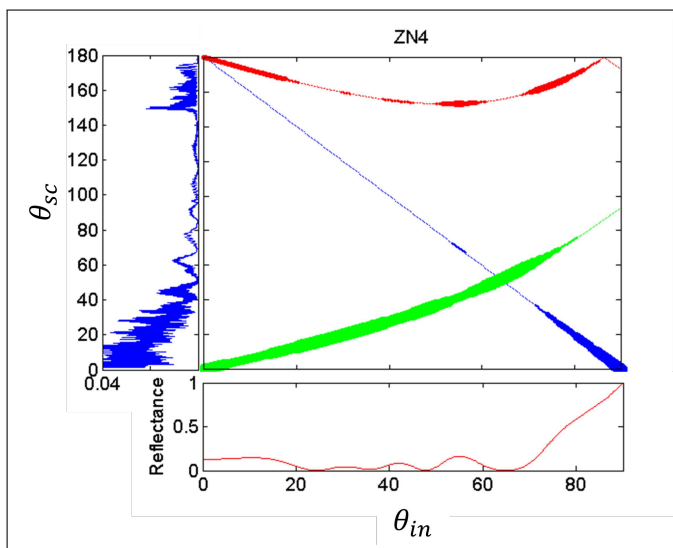


Fig. 11. Augmented scattering angle diagram for a Bragg fiber without a stopband, hence resembling scattering from bare fiber.

3. Luk'yanchuk B, Paniagua-Domínguez R, Kuznetsov AI, Miroshnichenko AE, Kivshar YS. Suppression of scattering for small dielectric particles: anapole mode and invisibility. *Philos Trans A Math Phys Eng Sci.* 2017.
4. Reupert, A., Heck, M., Nolte, S., Wondraczek, L., Angular Scattering Pattern of Femtosecond Laser-Induced Refractive Index Modifications in Optical Fibers. *Adv. Optical Mater.* 2020, 8, 2000633.
5. Fu, Y., Kuznetsov, A., Miroshnichenko, A. et al. Directional visible light scattering by silicon nanoparticles. *Nat Commun* 4, 1527 (2013).
6. G. Tao, J. J. Kaufman, S. Shabahang, R. R. Naraghia, S. V. Sukhov, J. D. Joannopoulos, Y. Fink, A. Dogariu, and A. F. Abouraddy, "Digital design of multimaterial photonic particles," *PNAS* 113(25), 6839–6844 (2016).
7. Khudiyev, T., Huseyinoglu, E., Bayindir, M. Non-resonant Mie scattering:

Emergent optical properties of core-shell polymer nanowires. *Sci Rep* 4, 4607 (2014).

8. Li, Y., Wan, M., Wu, W. et al. Broadband zero-backward and near-zero-forward scattering by metallo-dielectric core-shell nanoparticles. *Sci Rep* 5, 12491 (2015).
9. Yuan, W., Zhou, N., Shi, L., Zhang, K-Q. Structural Coloration of Colloidal Fiber by Photonic Band Gap and Resonant Mie Scattering. *ACS Appl. Mater. Interfaces* 2015, 7, 25, 14064–14071
10. Erwin, W. R., Bardhan, R. Directional Scattering and Sensing with Bimetallic Fanocubes: A Complex Fano-Resonant Plasmonic Nanostructure. *J. Phys. Chem. C* 2016, 120, 51, 29423–29431.
11. Runmin Li, Xin Zhou, Mingcheng Panmai, Jin Xiang, Haiying Liu, Min Ouyang, Haihua Fan, Qiaofeng Dai, and Zhongchao Wei, "Broadband zero backward scattering by all-dielectric core-shell nanoparticles," *Opt. Express* 26, 28891-28901 (2018)
12. W. Liang, Y. Xu, Y. Huang, A. Yariv, J. G. Fleming, and S.-Y. Lin, "Mie scattering analysis of spherical Bragg "onion" resonators," *Optics Express*, vol. 12, pp. 657-669, 2004/02/23 2004.
13. Y. Xu, W. Liang, A. Yariv, J. G. Fleming, and S.-Y. Lin, "Modal analysis of Bragg onion resonators," *Optics Letters*, vol. 29, pp. 424-426, 2004/03/01 2004.
14. D. D. Smith and K. A. Fuller, "Photonic bandgaps in Mie scattering by concentrically stratified spheres," *Journal of the Optical Society of America B*, vol. 19, pp. 2449-2455, 2002/10/01 2002.
15. Z. Naqvi, M. Green, K. Smith, C. Wang, P. Del'Haye, and T-H. Her, "Uniform Thin Films on Optical Fibers by Plasma-Enhanced Chemical Vapor Deposition: Fabrication, Mie Scattering Characterization, and Application to Microresonators," *J. Lightwave Technol.* 36, 5580-5586 (2018)
16. M. Kerker and E. Matijević, "Scattering of Electromagnetic Waves from Concentric Infinite Cylinders*," *Journal of the Optical Society of America*, vol. 51, pp. 506-508, 1961/05/01 1961.
17. J.-P. Schaefer, Implementierung und Anwendung analytischer und numerischer Verfahren zur Lösung der Maxwellgleichungen für die Untersuchung der Lichtausbreitung in biologischem Gewebe. Open Access Repositorium der Universität Ulm. Dissertation, PhD, Ulm, 2011.
18. Z. Wu & L. Guo, Electromagnetic Scattering From a Multilayered Cylinder Arbitrarily Located in a Gaussian Beam, a New Recursive Algorithm, *Journal of Electromagnetic Waves and Applications*, 725-726 (1998)